Limited View Angle Iterative CT Reconstruction

Sherman J. Kisner[a], Eri Haneda[a], Charles A. Bouman[a], Sondre Skatter[b], Mikhail Kourinny[b], and Simon Bedford[c]

[a]Purdue University, West Lafayette, IN, USA;
[b]Morpho Detection Inc., Newark, CA, USA;
[c]Astrophysics Inc., City of Industry, CA, USA

ABSTRACT

Computed Tomography (CT) is widely used for transportation security to screen baggage for potential threats. For example, many airports use X-ray CT to scan the checked baggage of airline passengers. The resulting reconstructions are then used for both automated and human detection of threats. Recently, there has been growing interest in the use of model-based reconstruction techniques for application in CT security systems. Model-based reconstruction offers a number of potential advantages over more traditional direct reconstruction such as filtered backprojection (FBP). Perhaps one of the greatest advantages is the potential to reduce reconstruction artifacts when non-traditional scan geometries are used. For example, FBP tends to produce very severe streaking artifacts when applied to limited view data, which can adversely affect subsequent processing such as segmentation and detection.

In this paper, we investigate the use of model-based reconstruction in conjunction with limited-view scanning architectures, and we illustrate the value of these methods using transportation security examples. The advantage of limited view architectures is that it has the potential to reduce the cost and complexity of a scanning system, but its disadvantage is that limited-view data can result in structured artifacts in reconstructed images. Our method of reconstruction depends on the formulation of both a forward projection model for the system, and a prior model that accounts for the contents and densities of typical baggage. In order to evaluate our new method, we use realistic models of baggage with randomly inserted simple simulated objects. Using this approach, we show that model-based reconstruction can substantially reduce artifacts and improve important metrics of image quality such as the accuracy of the estimated CT numbers.

Keywords: computed tomography, iterative reconstruction, Markov random field, limited view, transportation security

1. INTRODUCTION

While *computed tomography* (CT) has developed primarily in the context of medical applications, there has been increasing utilizing of CT systems for transportation security. For example, many airports have deployed X-ray CT systems as a central component of baggage screening. While the underlying theory is largely the same as for medical CT, a different set of constraints are associated with security CT systems, such as the physical size and diversity of the scanned objects, the maximum acceptable X-ray energy, and the scan time requirements. Such constraints present some new opportunities and challenges for the CT reconstruction problem.

Scan time is a particularly important constraint for many security screening systems in order to handle the large volume associated with a transportation environment. One strategy to reduce scan time in a CT system is to simply take measurements at a fewer number of view angles, but this is generally to the detriment of reconstruction quality due to the ill-posed nature of the inversion problem.[1] For example, the traditional *filtered backprojection* (FBP) algorithm typically produces severe streaking artifacts in the limited view problem, which can in turn affect the later stages of security screening.

Further author information:
S.J. Kisner: E-mail: kisner @ purdue.edu
C.A. Bouman: E-mail: bouman @ purdue.edu

Computational Imaging X, edited by Charles A. Bouman, Ilya Pollak, Patrick J. Wolfe, Proc. of SPIE-IS&T Electronic Imaging, SPIE Vol. 8296, 82960F
 · doi: 10.1117/12.917781

Recently, there has been growing interest in the use of model-based reconstruction techniques in CT security systems. Their potential to produce high-quality reconstructions is facilitated by their ability to incorporate knowledge of the physical and statistical properties of both the scanner and the targets. These include modeling of system geometry, uncertainty in the measurements, and prior knowledge about the solution. In particular, the modeling of the underlying image plays an important role in compensating for the missing data in the limited view problem.

One established class of model-based techniques applies a regularization on the solution through a *Markov random field* (MRF) prior model, describing the statistical distribution of a voxel given its neighbors. Such methods formulate the reconstruction as a maximization of the *posterior* distribution (of the image, given the measurements), or a *MAP* estimate. The optimization is typically solved using an iterative strategy[2] such as *iterative coordinate descent* (ICD).

The particular choice of MRF prior model has a strong influence on the character of the solution. A quadratic, or Gaussian MRF (GMRF) prior, provides for fast convergence but tends to over-regularize the solution. The *generalized Gaussian MRF*[3] (GGMRF) provides noise suppression while preserving edges in the image. A further generalization called the *q-generalized Gaussian MRF*[4] (qGGMRF) is even more controllable while providing for fast convergence.[5]

At present, only a small number of published studies have been dedicated to CT reconstruction for transportation security,[6,7] including the application of FBP[8] and algebraic reconstruction (ART).[9] In this paper, we evaluate the performance of model-based reconstruction for parallel beam CT in the context of transportation security. We investigate the effect of reconstruction with a limited number of projection angles, as well as the effect of background clutter on the accuracy of the attenuation coefficient estimates. The FBP algorithm is used as a baseline for comparison.

2. METHODS

2.1 Projection Model

We assume a linear forward projection model in which, in the noiseless case, the object density image, $x \in \mathbb{R}^M$, and the projections, $y \in \mathbb{R}^N$, are related by a sparse matrix operator A,

$$y = Ax \ . \tag{1}$$

The matrix coefficient A_{ij} represents the contribution of voxel j in forming projection element i. In a line-beam model, A_{ij} is calculated as the length of beam i that intersects voxel j. In a wide-beam model,[10] which accounts for the fact that photons are collected over a detector *area*, the coefficient A_{ij} is computed as the inner product of the projection of voxel j onto the face of sensor i, with a detector efficiency kernel which is typically a simple indicator function. All results presented in this study use the wide-beam model.

2.2 Iterative MAP reconstruction

In the statistical framework, we consider the image, x, and the projection measurements, y, as random vectors, and our goal is to reconstruct the image by computing the maximum *a posteriori* (MAP) estimate given by

$$\hat{x} = \underset{x \geq 0}{\operatorname{argmin}} \{ -\log p(y|x) - \log p(x) \} \tag{2}$$

where $p(y|x)$ is the likelihood function associated with the data model, and $p(x)$ is the prior distribution of x. Note we also include a positivity constraint on the solution.

In general, the received photon count, λ_i, corresponding to projection i follows a Poisson distribution with mean $\bar{\lambda}_i = \lambda_{T,i} e^{-A_{i*}x}$, where $\lambda_{T,i}$ denotes the input photon count for projection i, and A_{i*} denotes the i^{th} row of the projection matrix. Starting from the Poisson model, a second-order Taylor expansion can be used to approximate the log likelihood term by the following,[2]

$$\log p(y|x) \approx -\frac{1}{2}(y - Ax)^T D(y - Ax) + f(y) \tag{3}$$

where A is the forward projection matrix, D is a diagonal weighting matrix given by $\text{diag}\{\lambda_1, ..., \lambda_N\}$, and $f(y)$ is a function which depends on measurement data only. Note in this form, the photon count, λ_i, acts as a weighting coefficient for the error, $(y_i - A_{i*}x)^2$, associated with projection i (i.e. smaller photon counts are less reliable, so are weighted less in the cost framework).

We will consider a Markov random field for the prior model, $p(x)$, where we use a standard 8-point neighborhood. An MRF distribution is often defined implicitly in terms of conditional densities, but the Hammersley-Clifford theorem allows the joint density to be expressed as a Gibbs distribution of the following form,

$$p(x) = \frac{1}{z} \exp\left\{ - \sum_{\{s,r\} \in \mathcal{C}} b_{s,r} \rho(x_s - x_r) \right\} \tag{4}$$

where ρ is a positive and symmetric function called the *potential function*, $\mathcal{C}$ is the set of all pairwise cliques and z is a normalizing constant. The MAP solution then becomes,

$$\hat{x} = \underset{x \geq 0}{\text{argmin}} \left\{ \frac{1}{2} \|y - Ax\|_D^2 \; + \sum_{\{s,r\} \in \mathcal{C}} b_{s,r} \rho(x_s - x_r) \right\} \; . \tag{5}$$

In this study, we consider two different potential functions, $\rho(\cdot)$. The first is a quadratic, which corresponds to a Gaussian Markov random field (GMRF). So defining $\Delta = x_s - x_r$, we have,

$$\rho(\Delta) = \Delta^2 \; . \tag{6}$$

The second, is a q-generalized Gaussian MRF, or qGGMRF,[4] which has the form,

$$\rho(\Delta) = \frac{|\Delta|^p}{1 + |\Delta/c|^{p-q}} \; . \tag{7}$$

Generally, the qGGMRF potential allows more control over the behavior since $\rho(\Delta) \approx |\Delta|^p$ for small values of Δ (small voxel differences), and is proportional to $|\Delta|^q$ for large values of Δ. The c parameter controls the "transition point" between these two cases. Of particular interest are the cases where $1 \leq q \leq p$, which ensures convexity of the potential function. Common values to use are $p = 2$ (quadratic near zero), and q close to 1.

The reconstruction is computed by minimizing the expression in Eq. (5). We compute the solution by iterative coordinate descent (ICD) which minimizes the cost with respect to each voxel serially. Note because of our choice of priors, the global cost function is convex and ICD is ensured to converge to the global minimum.

2.3 Filtered Backprojection

For comparison, reconstructions are also computed using *filtered backprojection*. The filter employed in these reconstructions has a ramp frequency response multiplied by a Hamming window, and a cutoff frequency of 0.8 times the Nyquist rate. Source code for this reconstruction software is available for download (See Ref. 11).

2.4 Sinogram Data

So that we can evaluate reconstructions with respect to ground truth, projection data is simulated in this study by applying the forward projector in Eqn. (1) to a clean high-resolution scan of a duffel bag. Since we are principally interested in examining the effect of a reduced number of view angles, and the effect of clutter in the image, no photon noise is incorporated for this study.

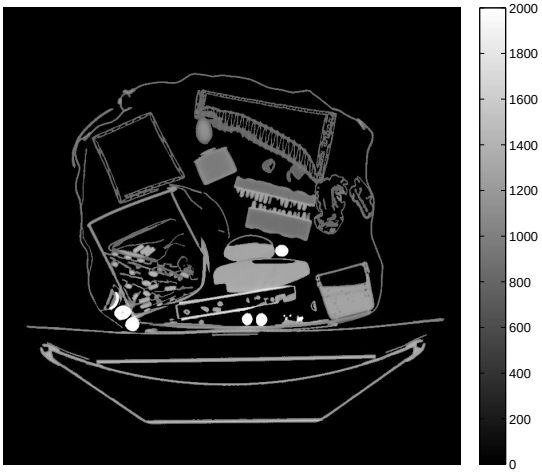

Figure 1. High resolution CT bag scan used as ground truth for the current experiment. Gray scale is in offset Hounsfield units (HU), where Air=0 HU. The original CT image contained reconstruction artifacts due the diversity in composition and morphology of items in the bag, which were removed by masking out the background (set to 0 HU), and retaining only the visible objects. A linear wide-beam projector was then used to generate sinogram data for the current analysis.

3. RESULTS

This section will present both qualitative and quantitative analyses on the accuracy of model-based reconstruction. Figure 1 shows the cluttered bag-scan image used to generate simulated projection data for the analysis. The original CT image itself contained reconstruction artifacts due the diversity in composition and morphology of items in the bag, which were effectively removed by masking out the background, and retaining only the visible objects. The full set of image data and reconstruction parameters are summarized in the Appendix.

3.1 Effect of Limited View Angles

Figure 2 shows the reconstructions after forward projecting the bag scan of Fig. 1 at a limited number of equally spaced view angles between 0 and 180 degrees. Illustrated is the effect of reducing the number of view angles on reconstruction by filtered backprojection (FBP), and by iterative model-based reconstruction using a Gaussian Markov random field (GMRF) prior, and a q-generalized Gaussian MRF prior (qGGMRF). The corresponding *root mean square error* (RMSE) from ground truth for each of these reconstructions is listed in Table 1. The RMSE was computed from only those voxels having a density greater than air in the ground truth image.

Table 1. Root mean square error of reconstructions in Fig. 2. Units are offset Hounsfield (air=0).

no. of views	FBP	GMRF	qGGMRF
64	481.0	237.8	112.8
32	628.4	361.1	277.1
16	746.2	498.9	453.8
8	854.4	607.1	598.5

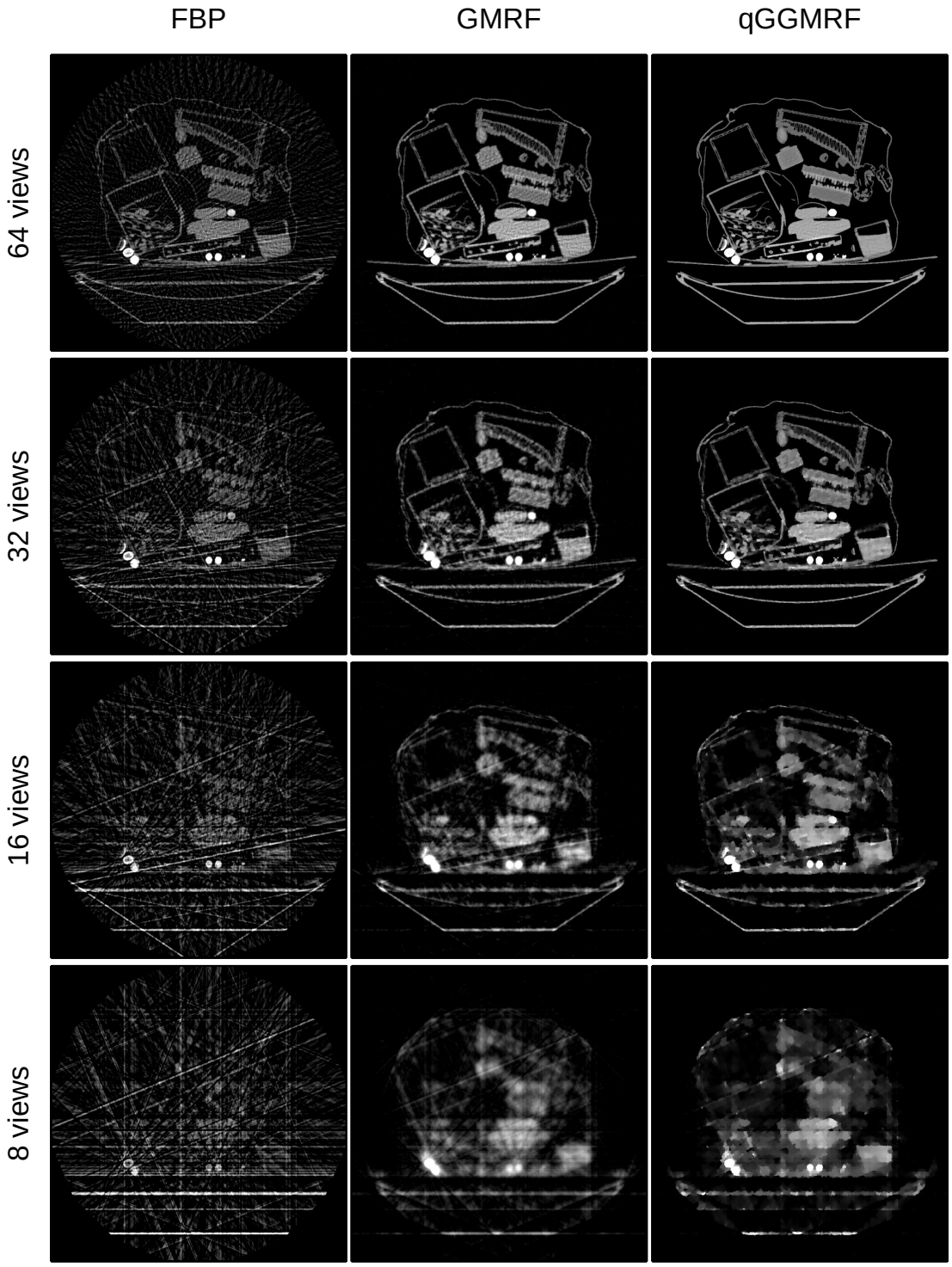

Figure 2. Image reconstructions from limited view angle projection data. Four parallel projection data sets are considered, containing 64, 32, 16, and 8 view angles, uniformly spaced between 0 and 180 degrees. Reconstructions include filtered backprojection (FBP) and iterative MAP reconstruction using a Gaussian Markov random field prior (GMRF), and a q-generalized Gaussian MRF prior (qGGMRF). The gray scale range for all results shown is [0,2000] HU, as in the ground truth image of Fig. 1.

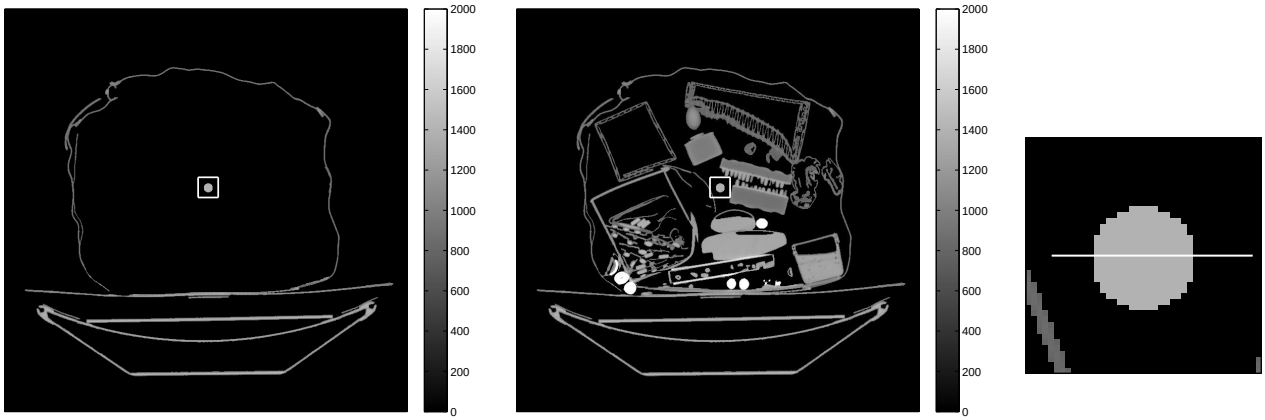

(a) Low clutter scene (b) High clutter scene (c) Target

Figure 3. Ground truth images for investigating the effect of clutter on CT reconstruction accuracy. The bag contents from the ground truth image in Fig. 1 have been masked out to create a *low clutter* scene in (a). For evaluation, a synthetic target of uniform value (1400 HU) has been added, as highlighted by the box near the center of the low and high clutter scenes. A close-up of the target in (c) also shows a reference line highlighting voxels that will be examined in the experiment.

3.2 Effect of Clutter on CT Accuracy

To examine the effect of image "clutter" on the accuracy of CT number estimates, we modified the ground truth image of Fig. 1 in two respects. First, the contents of the bag scan were masked out to produce a *low clutter* scene, and we consider the original image as a *high clutter* scene. Second, we inserted a single round 1.7 cm diameter target of a known uniform CT value (1400 HU) somewhere inside the perimeter of the bag. Figures 3(a) and 3(b) illustrate this for the low and high clutter scenes, and 3(c) shows a close-up of the target.

Two experiments were performed. In the first, we produced 32 view angle parallel projection data from the images shown in Figures 3(a) and 3(b) (without the highlighting box). Reconstructions were computed using FBP and iterative MAP reconstruction using the GMRF and qGGMRF priors. A close-up of the reconstructions around the target region are shown in Figure 4, which can be compared to the ground truth shown in Figure 3(c). Figure 5 shows the reconstructed CT numbers for voxels along the reference line shown in Figure 3(c).

In the second experiment we calculated the average accuracy of the reconstructed target voxels after placing the target at various locations in the bag. Specifically, in each trial we (1) place the synthetic target at a random location inside the bag perimeter, (2) forward project to produce a 32 view angle sinogram, (3) reconstruct, and (4) calculate the average deviation of the target voxels from the true value, as well as the root mean square of the deviations. Table 2 summarizes the results of this procedure averaged over 60 trials of random placement.

Table 2. Statistics for the reconstructed CT numbers for a randomly placed synthetic target. The values were computed by averaging over 60 trials of placing a round 1.7cm uniform target (1400 HU) at random locations within the bag perimeter in the ground truth images (See Fig. 3). The *Dev.* is the average deviation of reconstructed target voxels from the true value. Similarly, the *RMSE* is the root mean square deviation from the true target value. All values are in offset Hounsfield units (air=0).

	Low clutter		High clutter	
	Dev.	RMSE	Dev.	RMSE
FBP	-895.1	899.1	-647.8	702.7
GMRF	-157.2	280.4	-179.8	332.7
qGGMRF	-14.2	25.8	-87.3	209.2

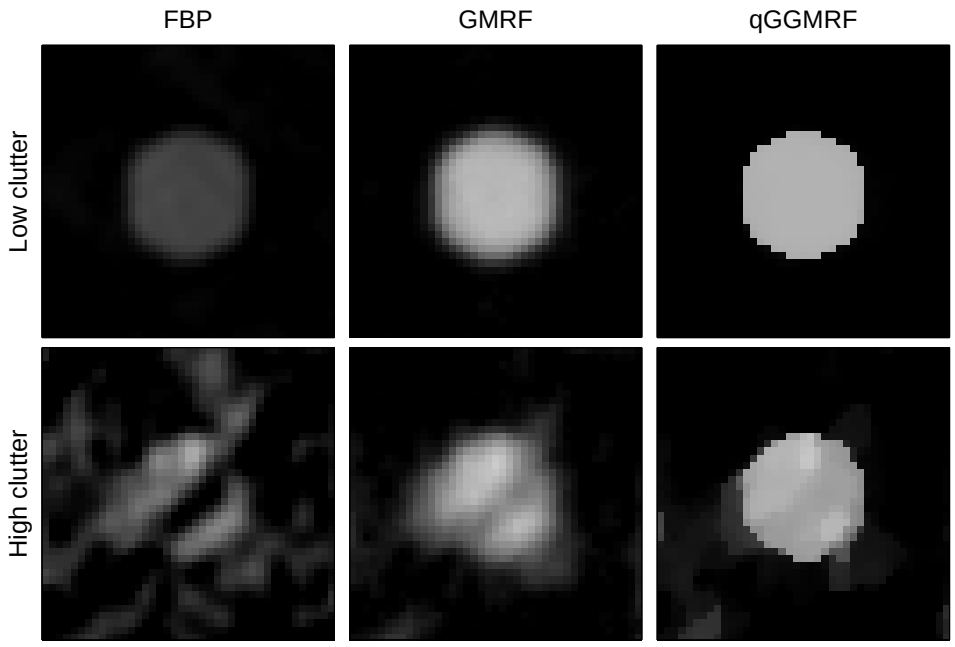

Figure 4. Reconstructions zoomed to the target area indicated in Figs. 3(a) and 3(b). All results are from 32 view angle parallel projection data, the top row generated from the low clutter scene of Fig. 3(a), and the bottom row from the high clutter scene of Fig. 3(b).

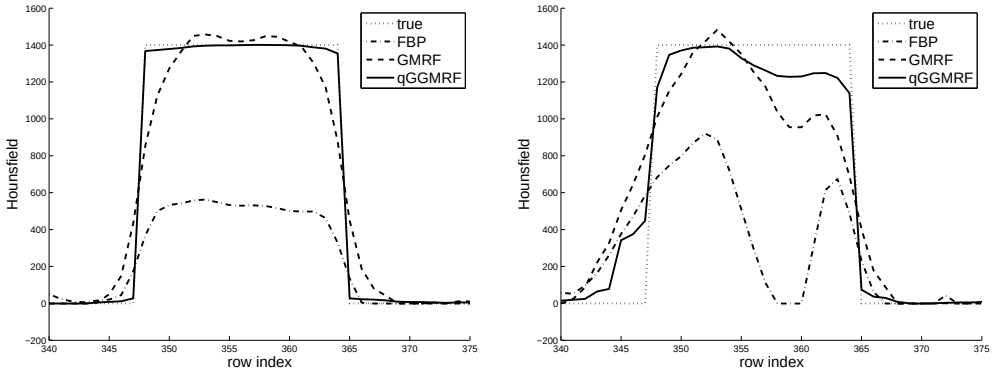

(a) Low clutter background (b) High clutter background

Figure 5. CT values from limited view reconstructions of Fig. 4 for voxels along a line through the center of the target region (See Fig. 3(c)). Also shown are the true voxel values from ground truth.

4. DISCUSSION

The most apparent advantage of model-based reconstruction from Figure 2 is a reduced susceptibility to streaking artifacts, whereas FBP quickly devolves into streaks as the number of views becomes small. While streaking patterns can be seen in dense regions of the MAP-GMRF result at 64 views, the spatial extent of the streaks is much more localized than in FBP, and the regularization of the qGGMRF prior further reduces these dramatically.

In fact, for each data set in Figure 2 the qGGMRF prior produces a result with less structured error and a clearer edges that the GMRF prior. However, for extremely low view angles such as the 8-views case, the advantage of the qGGMRF over GMRF is minimal because the edge locations are not always accurate. These points are also reflected in the RMSE values listed in Table 1. In each case, the qGGMRF RMSE is smaller than the GMRF RMSE, with the difference becoming less significant as the number of views decreases.

Of note in Table 1 is the result that, in the mean square sense, MAP-qGGMRF produces a more accurate reconstruction than FBP using only a quarter of the number of views. Specifically, the RMSE of qGGMRF at 16 views is smaller than that of FBP at 64 views, and qGGMRF at 8 views is smaller than FBP at 32 views. If this result generalizes, this is a particularly significant consideration since the number of views can have a direct correlation to system cost, scan time, and reconstruction time. Of course this marked difference in RMSE does not necessarily translate in the qualitative sense because visual inspection can somewhat compensate for the streaking in FBP. It should also be noted that one reason for the relatively high RMSE in the FBP reconstructions is a general underestimation of the CT numbers (which is apparent in Figure 2) partly due to image energy dispersal in the streaking. Presumably an appropriate image-dependent rescaling could be employed to provide a degree of compensation for this.

The 32-view synthetic target experiment of Figs. 4 and 5 reinforces several of the above observations. Namely, MAP-qGGMRF produces a much more accurate reconstruction in terms of both CT numbers overall, and in terms of edge clarity. The low clutter scene results in effectively no visible streaking in any case, with qGGMRF producing very accurate CT numbers and very little blurring of the target boundary. In the high clutter scene, FBP fully splits the target into two disjoint objects, while the GMRF prior produces a recognizable object but with highly non-uniform CT numbers. The qGGMRF prior produces a significantly more uniform reconstruction of the target and reproduces the edges with remarkable accuracy by comparison.

The results of the random placement experiment summarized by Table 2 are a more general confirmation of the observations about the reconstructions in Fig. 4. Since the target position is allowed to vary, the results are not strongly dependent on any particularly strong streaking artifacts caused by the metallic objects in the image. Of note is the factor of 10 improvement in the accuracy in the low clutter scene, going from the GMRF to the qGGMRF prior. As observed in Fig. 5(a), this is due to the much more accurate edge reconstruction afforded by the qGGMRF model. Similar, while not as dramatic, improvements are produced for the high clutter scene.

5. CONCLUSION

This paper presented the application of iterative model-based reconstruction on limited view angle parallel projection data, generated from a typical bag scan. We compared MAP reconstructions using two different prior models, a Gaussian Markov random field (GMRF) and a q-generalized Gaussian Markov random field (qGGMRF), to the standard filtered backprojection algorithm. Qualitative and quantitative measures demonstrated potentially great strengths in model-based reconstruction applied to transportation security, both in terms of reconstruction of form and in the CT number accuracy.

APPENDIX A. IMAGE AND RECONSTRUCTION PARAMETERS

Sinogram parameters	no. of angles	{64,32,16,8}
	no. of translations	800
	Δ_θ	180/no_angles deg
	detector width	1 mm
Image geometry	xdim	800 pixels
	ydim	800 pixels
	field of view	80 cm
	voxel size	1 mm
qGGMRF parameters	p	2.0
	q	1.0
	c	15.0 HU

Table 3. Image and Reconstruction Parameters

ACKNOWLEDGMENTS

This work is supported and funded by the Department of Homeland Security, Science and Technology Directorate (Explosives Division and Transportation Security Laboratory). The authors would also like to thank General Electric for providing the CT scan used in this study.

REFERENCES

[1] Davison, M. E., "The ill-conditioned nature of the limited angle tomography problem," *SIAM J. Appl. Math.* **43**, 428–448 (1983).

[2] Sauer, K. and Bouman, C., "A local update strategy for iterative reconstruction from projections," *IEEE Trans. on Signal Processing* **41**(2), 534–548 (1993).

[3] Bouman, C. and Sauer, K., "A generalized Gaussian image model for edge-preserving MAP estimation," *IEEE Trans. on Image Processing* **2**(3), 296–310 (1993).

[4] Thibault, J.-B., Sauer, K., Bouman, C., and Hsieh, J., "A three-dimensional statistical approach to improved image quality for multi-slice helical CT," *Medical Physics* **34**(11), 4526–4544 (2007).

[5] Yu, Z., Thibault, J., Bouman, C., Sauer, K., and Hsieh, J., "Fast model-based X-Ray CT reconstruction using spatially non-homogeneous ICD optimization," *IEEE Trans. on Image Processing* **20**(1), 161–175 (2011).

[6] Smith, R. C. and Connelly, J. M., [*Aspects of Explosives Detection, Chapter 7 - CT Technologies*], Elsevier (2009).

[7] Ying, Z., Naidu, R., and Crawford, C., "Dual energy computed tomography for explosive detection," *Journal of X-Ray Science and Technology* **14**(4), 235–256 (2006).

[8] Riveros, E., "The digital radiographic and computed tomography imaging of two types of explosive devices," *Applied Radiation and Isotopes* **57**(6), 861–865 (2002).

[9] Zhang, H., Sun, Y., and Wei, L., "Explosives detection method based on improved algebraic reconstruction technique," in [*Intelligent Control and Automation, 2008*], 1764–1767 (June 2008).

[10] Buzug, T., [*Computed Tomography: From Photon Statistics to Modern Cone-Beam CT*], Springer (2010).

[11] Bouman, C. A., "Tomography software," Available from http://www.ece.purdue.edu/~bouman/software/tomography (2011).